

# 1 Chemical Reactions

*Renu Sharma*

Center for Nanoscale Science and Technology, National Institute of Science and Technology,  
100 Bureau Drive, Gaithersburg, MD 20899-6201, USA

## 1.1 INTRODUCTION

Understanding the chemical reaction processes involved in materials synthesis and their functioning is central to our ability to control their performance. A number of technologies such as thermogravimetry analysis, calorimetry, temperature-programmed reduction *etc.* are routinely used to determine the optimum reaction conditions such as temperature and pressure. Similarly, X-ray diffraction, Raman spectroscopy, infrared spectroscopy, scanning probe microscopy (SPM), scanning electron microscopy (SEM), transmission electron microscopy (TEM), and energy dispersive x-ray spectroscopy (EDS) are examples of some of the techniques employed to characterize reactants and products before and after the reaction. However, it has been clear for some time that measurement performed on reactants and products are often not sufficient to determine subtle changes in the reaction mechanisms and kinetics. Therefore *in situ* observations of chemical reactions using the various techniques mentioned above are now commonly employed.

The need for nanoscale measurements stems from the rigorous control of synthesis conditions that is essential for nanofabrication. Continued progress in nanotechnology requires that nanomaterials with a desired property must be produced in significant quantities. Moreover, the properties of nanomaterials are often controlled by their nanoscale structure and will be adversely affected by any structural modification occurring during their operation. Since TEM is one of the most powerful techniques for atomic scale characterization, a number of modifications to the TEM sample holders and to the column have been made over the years that enabled us to follow chemical reaction kinetics and mechanisms at nanoscale. The insights provided by these observations can be exploited to facilitate robust scaling of nanoscale synthesis processes to the manufacturing levels. The quest to observe chemical reactions at or near atomic scale has been the driving force behind recent advances in TEM specimen holders as well as TEM columns.[1-13] For example, solid-phase chemical reactions resulting from increases or decreases in temperature can be observed using suitable heating or cooling holders. More extensive

modifications of the TEM column and/or the holders permit us to follow *gas*-solid reactions at the atomic level.

This chapter will provide a brief description of currently available instrumentation, the types of chemical reactions we can follow, experiment planning strategies, and examples of using TEM related techniques to measure structural and chemical transformations as well as reaction kinetics. A discussion of the limitations and directions for future development will also be given.

## 1.2 INSTRUMENTATION

Transmission electron microscopes require high vacuum (better than  $1.34 \times 10^{-4}$  Pa ( $10^{-6}$  Torr) in order to avoid loss of image contrast/resolution arising from the multiple scattering of the incident electrons by the gas molecules. Recent developments in instrumentation have made it possible to introduce gas or liquid, confined to the sample area, to study various types of gas-solid or liquid-solid reactions at the nanoscale without losing image contrast or resolution.

Broadly speaking there are two types of modifications that have been successfully employed for *in situ* observations: specialized sample holders or differentially pumped TEM columns. Holders for heating and cooling are commercially available and have been extensively used to follow solid-state reactions such as phase transformations, decomposition, reduction, de-hydroxylation, *etc.* Tan et al. have also incorporated the capability to measure electric field effects on the movement of domain boundaries in piezoelectric and ferroelectric single crystals at elevated temperatures.[14, 15]

Several other research groups have also constructed holders that confine fluids using electron transparent windows. The basic principle of the windowed design is shown in Figure 1, where the sample is sandwiched between two electron transparent windows and the flow of liquid or gas can be regulated using external pumps. Ross et al. have used such custom-built windowed holders to follow the etching process in Si by HF and the nucleation and growth of Cu particles during electrolysis of copper sulfate solution under static conditions (without flow).[16, 17]

Similar TEM holders have also been successfully employed to follow particle motion in liquid.[18, 19] Figure 2 shows the schematic of a commercially available windowed holder.[20] Windowed grids are sealed to the cap plates on top and bottom using o-ring seals (Figure 2). The main drawback of the windowed design is that the window material must be thick enough, typically 50 nm, to withstand the pressure differential between the gas/liquid and microscope vacuum. The additional thickness of the confining windows tends to degrade the spatial resolution of the image, typically making high-resolution (lattice) imaging impossible. However,

Creemer et al. [11] have recently demonstrated high-resolution images of catalyst particles in  $1 \times 10^5$  Pa (approximately 760 Torr) of  $H_2$  at 500 °C using a windowed holder. This holder, which they call a nanoreactor, is based on microelectromechanical system (MEMS) technology, and features micrometer scale gas flow channels and a heating device in a silicon chip, as shown in Fig. 3. The high-resolution performance was achieved by thinning the electron-transparent windows locally (approximately 10 nm diameter) to 10 nm thickness.

Alternatively, a gas-injection system can be incorporated into a heating holder such that a small amount of gas can be directly delivered in the vicinity of the samples, which are mounted on a wire-heating holder, as shown in Figure 4.[9] This design has been successfully applied to follow catalytic reactions and the growth of  $W_{18}O_{49}$  nanowires.[10, 21, 22] Such an approach relies on careful control of the gas flow to avoid the degradation of the column vacuum. Therefore, modifying the TEM column to follow gas-solid interactions is currently more popular than modified holders as they allow high pressure to be achieved for an unobstructed view of the sample. Also, most of the modified holders for heating, cooling, indentation, tomography, *etc.* can be used in these microscopes. The main drawback of a differentially pumped system is that the upper limit on achievable temperature and pressure is 900 °C and  $2.5 \times 10^{-3}$  Pa ( $1.9 \times 10^{-5}$  Torr), respectively.[23] Therefore we may not be able to achieve the same reaction conditions in the TEM column as used for most industrial applications.

Currently two types of TEM, with modified column, capable of *in situ* observation of gas-solid interactions are commercially available. First are ultra-high vacuum TEMs, where a gas injection system is incorporated in the TEM column to introduce low pressures, below  $1.33 \times 10^{-4}$  Pa ( $10^{-6}$  Torr), of gas and/or vapor. Such microscopes have been successfully used to follow the nucleation and growth of Ge islands on Si,[24] growth of Si, Ge and InP nanowires,[25-30] nitridation of  $Al_2O_3$ ,[31] growth of carbon nanotubes,[32] *etc.* These microscopes are ideally suited for studying gas interactions with clean surfaces due to the low base pressures ( $1.33 \times 10^{-8}$  Pa ( $10^{-10}$  Torr)), readily achieved in the column. Second are differentially pumped TEMs that employ additional pumping in the objective pole-piece area to enable the introduction of gas into the sample region. These are usually referred to as environmental TEMs or ETEMs. This design was first proposed by Swann and Tighe [4] and has been improved constantly since then.[1, 3, 7, 33-35] The basic principal of a differential pumping system is shown in Figure 5 where gas is introduced in the sample area and its leak rate to the rest of the column is reduced by using apertures above and below the sample area, and pumping the gas leaking through these apertures using a turbomolecular pump (TMP), (Figure 5, 1<sup>st</sup> level of pumping). The gas leak rate is further reduced by introducing another TMP attached to the second outlet between the condenser

aperture and top of the pole-piece for the upper half of the column, and between the selected area aperture and the differential pumping aperture, located above the viewing screen (Figure 5, 2<sup>nd</sup> level of pumping) for the lower half of the column. The pre-gun area is further evacuated using another pump, typically an ion pump (Figure 5, 3<sup>rd</sup> level of pumping). As a result, samples can be exposed to  $1.33 \times 10^3$  Pa to  $2.66 \times 10^3$  Pa (10 Torr to 20 Torr) of gas pressure while the gun chamber is kept at  $1.33 \times 10^{-8}$  Pa ( $10^{-10}$  Torr). During the last 20 years, a number of research groups have worked on this design and such microscopes are now commercially available. Details about the design and functioning of these microscopes have been published in a number of reviews [23, 36-40] and will not be covered in this chapter.

## 1.3 TYPES OF CHEMICAL REACTION SUITABLE FOR TEM OBSERVATION

We can broadly categorize chemical reactions based on the physical state of the reactants and products, i.e., gas, liquid or solid. TEM is often most suited to characterize solids; therefore one of the reactants or products should be solid so that the structural and chemical changes occurring during the reaction can be followed using electron diffraction, imaging and spectroscopic techniques. The following sections provide a short description of reaction types studied to date.

### 1.3.1 Oxidation and reduction (Redox) reaction

Oxidation is one of the most commonly occurring reactions with everyday examples including the rusting of Fe and discoloration of Cu. Oxidation and reduction reactions are also fundamental to the function of a number of technologically important processes for energy generation and storage such as fuel cells, electrochemical cells, photo-catalysts, *etc.* Many of these processes involve oxidation/reduction cycles that are generally referred as redox reactions. An important example of such a reaction is functioning of three-way catalyst used in automobile exhaust system. This catalyst system typically consists of Pt or Rh nanoparticles supported on ceria-zirconia mixed oxides. The function of a catalytic convertor is to convert pollutant gasses ( $\text{NO}_x$ , CO and unreacted hydrocarbons) into relatively benign products ( $\text{N}_2$ ,  $\text{CO}_2$  and  $\text{H}_2\text{O}$ ). During the process, ceria from the support is either reduced to give lattice oxygen to convert CO to  $\text{CO}_2$  and unreacted hydrocarbons to  $\text{CO}_2$  and  $\text{H}_2\text{O}$ , or oxidized by converting  $\text{NO}_x$  to  $\text{N}_2$ . [41, 42] The redox process is accompanied by changes in the chemical composition and structure of ceria support. *In situ* observations of individual nanoparticles have revealed that the redox behavior is controlled by their chemical composition. [43] Details of the experimental protocol

for this reaction are given in section 1.5.2 of this chapter. The redox behavior of Au-Cu single crystals is described in chapter XX of this book.

### 1.3.2 Phase Transformations

The term phase transformation generally refers to transitions of states of matter, i.e. from solid to liquid to gas or vice versa. However, when discussing solids, the phrase describes a change in the atomic positions such as occurs during the crystallization of amorphous material or martensitic atomic displacement during the quenching of a steel. Such transformations often are accompanied by changes in material properties; for example, the band gap in TiO<sub>2</sub> changes from 2.98 eV to 3.2 eV as result of the structural transformation from the rutile to the anatase with temperature.[44] Similarly, the change in magnetization configuration in the ferromagnetic Ni<sub>2</sub>MnGa shape memory alloy is accompanied by a cubic-to-tetragonal phase transformation at low temperatures.[45] Tsuchiya et al [46] have also observed formation of intermediate structure in Ni-Mn-Ga alloys using *in situ* electron diffraction. These studies generally combine Lorentz microscopy observations with electron diffraction to obtain images of magnetic domain structures during heating or cooling. The effect of electric fields on piezoelectric and ferroelectric transformation has also been observed using a TEM holder capable of heating samples as voltages of up to 600 V were applied. Tan et al. have used this holder to determine the relationship between structural transformations and materials properties in Nb-doped lead zirconium titanate (PZT).[47]

### 1.3.3 Polymerization

During the last century, polymers have found application in everyday products such as clothing fabric, ropes, plastics, *etc.* Polymers are long covalently bonded chains consisting of multiple repetitions of relatively small organic molecules that act as a repeat unit. Formation of these large molecules is termed polymerization and is often assisted by a catalyst. Understanding the reaction process is fundamental to controlling the reaction conditions for maximum yield, control of molecular weight, polydispersity, *etc.* Oleshko et al. have used an ETEM to follow the synthesis mechanism of polypropylene from propylene using a Ziegler-Natta catalyst.[48, 49]

### 1.3.4 Nitridation

Epitaxial growth of nitride films is often achieved by direct nitridation of III-V materials that have been deposited on a suitable substrate such as sapphire. The presence of impurities like

oxygen has been reported to degrade the functional properties of nitride films. Yeadon et al. have used an ultra-high vacuum TEM with a gas injection system to follow the formation of AlN from Al<sub>2</sub>O<sub>3</sub> films by heating the samples to 950 °C in NH<sub>3</sub>. [31] Based on their observation, they were able to propose a diffusion-limited reaction model involving transport of oxygen and nitrogen ions through the AlN epilayer growing between the free surface and the unreacted  $\alpha$ -Al<sub>2</sub>O<sub>3</sub>. The nitridation reaction is also a key process in the production of integrated circuits in the semiconductor industry. In order to stop the metal used for interconnects (on-chip wiring) such as Cu, Cr or Ti from diffusing into the Si substrate and forming unwanted silicides at high (operating) temperatures, Ti or Cr nitride is used as a barrier layer. The nitridation reactions of these metals have been studied by recording time and temperature resolved selected area electron diffraction as the samples were heated in  $\approx$  266 Pa (2 Torr) of NH<sub>3</sub> (a nitrogen source) in an ETEM. [50] Time- and temperature-resolved selected area diffraction patterns show that the nitridation temperature for Cu-Ti thin films decreases with increasing Cu content in the films. Measured reaction rates, obtained from low magnification images, also agree with the reaction-controlled model for nitridation reaction. [51]

### 1.3.5 Hydroxylation and De-Hydroxylation

Water plays an important role in many naturally occurring reactions. For example clays or minerals, such as brucite and semactite can intake (hydroxylate) or give-up (de-hydroxylate) water as the environmental conditions change. The phenomenon results in structural transformation of materials as they are converted from oxide to hydroxide and back to oxide. De-hydroxylation generally occurs upon heating while hydroxylation can occur at room temperature. It has been shown that hydroxylation processes depend upon the structure and morphology of the starting materials. [52, 53] For example, we have shown that the hydroxylation rate for crystalline magnesium oxide (MgO) cubes (5 to 10 nm) is much lower than for amorphous MgO nanoparticles (1 to 5 nm) freshly prepared by de-hydroxylation of magnesium hydroxide (Mg(OH)<sub>2</sub>). [54]

Water molecules in the atmosphere are also responsible for the deliquescence and efflorescence of atmospheric nanoparticles. Freney et al. have used the ETEM to understand the effect of humidity, particle size and chemical nature of atmospheric particles on deliquescence and efflorescence phenomena relevant to aerosols. [55, 56] Their results provide new data for aqueous electrolytes that aid in our understanding of atmospheric science. [57, 58]

### 1.3.6 Nucleation and Growth of Nanostructures

One approach to effective use of 1-D nanostructures, such as nanotubes and nanowires in devices, is to synthesize them *in situ* during the device fabrication process in such a way that they have the precise electronic properties required. Understanding the nucleation and growth mechanisms is an essential step for optimizing their synthesis conditions. During the last decade, *in situ* TEM observations have been extensively used to understand the nucleation and growth of a variety of nanoparticles, nanowires and nanotubes.[27, 30, 59-66] Growth mechanisms for oxide nanostructures such as  $W_{18}O_{49}$  nanowires [22] and BiO whiskers [67] have been revealed using a gas-injection heating holder.

Figure 6a shows a series of images, extracted from a digital video, recorded as a small pressure (0.013 Pa ( $10^{-4}$  Torr)) of disilane ( $Si_2H_4$ ) was introduced into the ETEM column over a Au/ $SiO_2$  thin film sample heated to 590 °C. It is clear from these images that the Si nanowires nucleate from supersaturated Au-Si eutectic liquid. Careful measurements show (Figure 6b) that the incubation period (R) is dependent on the Au particle size (cross-sectional area ( $A_0$ )) with wires nucleating from small particles earlier than from the large particles.[27, 30] Based on the data shown in Figure 6b, it can be concluded that the incubation period is approximately equal to the square root of the cross-sectional area or radius of the particles ( $S \sim \sqrt{A}$ ).[30]

## 1.4 EXPERIMENTAL SET-UP

It is imperative to emphasize that for *in situ* TEM observations of chemical reactions, the column acts as both reaction cell and characterization tool. In other words, we perform our experiments in the TEM column and characterize reactants and products concurrently; therefore, we need to pay special attention to the choice of TEM grid/support material, heating/cooling holders, and the possible interactions of ambient gas (liquid) with these components. Moreover, it is important to evaluate the effect of the electron beam on the reaction path. In the following section, some important factors to consider before performing *in situ* TEM experiments are given.

### ***Reaction of ambient environment with various TEM components***

It is important to know the nature of materials used for various components of your microscope column and specimen holders, such as the body of the holder, body of the heating furnace, washers, wiring material, etc. Some of this information may be proprietary and therefore not readily available. In this case, consult with the manufacturer to make sure that the liquids or gasses to be used or produced during reaction will not harm your instrumental components. For example, Ta heating holders will oxidize when exposed to oxygen or air at high temperature, and

Pt heating wires will form silicides when heated above 600 °C in the presence of silane or disilane. Also, consult the relevant phase diagrams to make sure that the experiments can be safely performed using the available instrumentation.

### ***Reaction of grid/support materials with sample or each other***

Special attention must be given to choice of the material for the specimen support (e.g., TEM grid). For example, Cu is one of the most commonly used TEM grid materials for loading samples. It is obvious that we should not use Cu grids for reactions above the melting point (1083 °C) but it has been shown that metal atoms can start to diffuse at temperatures as low as half the melting temperature (as measured in Kelvin; the T<sub>aman</sub> temperature), which is  $\approx 400$  °C for Cu. The diffusion of metal atoms onto the samples near or above the T<sub>aman</sub> temperature can affect the results. For example, we have found that the yield of carbon nanotube formation increased noticeably at  $\approx 500$  °C when Ni/SiO<sub>2</sub> catalyst was loaded directly onto Au grids instead of Ni grids, as shown in Figure 7. We believe that since our reaction temperature is above the T<sub>aman</sub> temperature for Au (396 °C), some Au atoms diffused to the catalyst particles and changed their reactivity. Controlled experiments with varying (0.1 mole fraction to 0.8 mole fraction) have confirmed that Ni doped with less than 0.2 mole fraction of Au increases the CNT yield considerably. Another example is of CO reacting with Ni grids above 800 °C to form nickel carbonyl, a volatile product.

### ***Temperature and pressure considerations***

The maximum achievable temperature first and foremost depends upon the modified heating holder and varies between 1000 °C and 1500 °C, depending upon the source and design. For example, Saka et al have designed holders that are stable above 1500 °C.[9] Allard et al have recently reported a heating holder capable of cycling temperatures from ambient to above 1000 °C in one millisecond.[13] The steady-state temperature at the sample using this holder is stable enough to allow the capture of atomic resolution images in TEM as well as in scanning transmission electron microscope (STEM) modes. Other heating holders are also commercially available with approximately the same temperature range.

However, for *in situ* observations of gas solid interactions, the temperature limit depends not only upon the heating holder, but also on the components of the TEM column. For example, some of the internal components of the commercially available differentially pumped environmental TEMs (ETEMs) or environmental scanning TEMs (ESTEMs) cannot withstand high temperatures. As gasses transport the heat from the sample to other parts of the column, the

upper limit for achievable temperature with gas flow is 900 °C in a modern commercial ESTEM, even if the heating holder is capable of achieving higher temperatures.

### ***Selecting appropriate characterization technique(s)***

It is important to note that all of the TEM-related techniques such as imaging (bright field, dark-field, low and high resolution), electron diffraction (selected area, convergent beam, and electron nano-diffraction), scanning transmission electron microscopy (annular dark-field and high angle-annular dark-field), electron energy-loss and energy-dispersive spectroscopy, tomography, holography etc. can be used for *in situ* observations. Some of these techniques can be combined within the same experiment, depending upon the temporal resolution of the desired technique relative to the reaction rate of the chemical process under observation. Ideally we should combine more than one technique to unequivocally identify each step of the reaction process. For example, structural information can be obtained from either diffraction patterns or high resolution images but we need to collect spectroscopy data to determine the chemical changes. Examples given in this chapter (and elsewhere in this book) can be used as guides for selecting a technique or a set of techniques that should be used to obtain as much information as possible for a given chemical reaction. However, we should keep in mind that the power of *in situ* TEM lies in providing atomic-scale information on the reaction mechanism, the relationship between local composition and reactivity, and the relationship between local structure and properties etc. and not the bulk behavior.

### ***Recording media***

Our ability to obtain useful information from *in situ* TEM imaging or spectroscopy data is strongly dependent upon available temporal resolution of the recording media. Both digital and analog cameras, currently available to record high-resolution images, are limited to frame rate of  $\approx 30 \text{ s}^{-1}$  (fps). Improving the time resolution for HREM imaging is not a trivial challenge as it depends upon both the detector efficiency and electron dose.[68] Typical beam currents are between 1 nA and 10 nA; assuming recording takes place at a video rate of 30 frames per second or 0.03 s/frame, the number of electrons per frame is between  $6 \times 10^9$  and  $6 \times 10^{10}$ . Assuming images have the standard National Television System Committee (NTSC) resolution of 440×480 pixels, there are on an average of 750 electrons per pixel. Assuming one wants to detect a minimum of 8 contrast levels, 64 electrons per pixel would be necessary on a perfect detector. In order to reduce the electron dose we need to improve the detection quantum efficiency (DQE) of the camera. Typical camera DQEs are between 0.07 and 0.7 across the spatial frequency and kV range of interest, thus requiring between 100 and 1000 electrons per pixel. This means that, at

the resolution and sensitivity of current cameras, we are already at (or close to) the practical limit of frame rate. Increasing image integration times is frequently not an option as the required dose may alter (damage) many samples of interest. Increases in either the frame rate or in the resolution in terms of number of pixels per frame will require improvements in detector sensitivity (DQE) and possibly also new designs for the illumination systems of microscopes to maximize beam current.

Recently, a group of researchers at Lawrence Livermore National Laboratory has modified the TEM column to incorporate laser pulses to initiate a transient process to be investigated, e.g., phase transformations or chemical reactions, and timed it with the electron probe, also stimulated by a laser pulse, precisely such that snap shots can be recorded with 15 ns temporal resolution.[69] This microscope has been successfully employed to understand thermal annealing processes in thin films and the laser ablation mechanism for synthesis of nanowires.[70]

The temporal resolution that can be achieved for spectroscopy is lower than that for imaging: 2 s to 10 s or more compared to 0.34 s for video imaging. Therefore, spectroscopy techniques are often used to analyze a sample before and then after a reaction, unless the process is sufficiently slow. However, the recent introduction of a new generation of the Gatan GIF Quantum series of imaging energy filters, which enables the efficient collection of spectra at rates of up to  $100\text{ s}^{-1}$  is beginning to help overcome this limitation.

### ***Independent verification of the results and the effect of electron beam***

Limitations of *in situ* TEM characterization include the effect of the electron beam and the low achievable signal statistics of the data. Moreover, as samples suitable for TEM are usually of nanometer-scale thickness they may not represent the reaction mechanisms as they occur in bulk materials. Also, the reactions conditions, such as temperature and pressure that can be produced in the TEM may not represent the real-life situation. Therefore, it is important to verify the thermodynamic and kinetic parameters using other techniques such as X-ray diffraction, thermogravimetric analysis, Raman spectroscopy, etc. Also, the structure and chemistry of reactants and products subjected to the same reaction conditions as used in the TEM should be tested on bulk samples.

## **1.5 AVAILABLE INFORMATION UNDER REACTION CONDITIONS**

In order to understand the reaction mechanisms, thermodynamics, and kinetics, we need to make different sets of measurements depending upon the information needed. Most of the studies

employ the TEM to record data from one or a combination of imaging and spectroscopy techniques used on a sample under reaction conditions. The following examples provide a guide to select the specific combination of techniques most suitable to follow a particular reaction process. Detailed information about individual reactions can be found in the references provided in this chapter and in other chapters of this book.

### 1.5.1 Structural modification

Identifying structural changes during a reaction is the most frequently used technique for following reaction mechanisms and/or paths. These changes may occur during any of the reactions mentioned in Section 1.3. Time- and temperature-resolved high-resolution imaging and/or electron diffraction can be used to determine changes in local structure. The time resolution is dependent on the recording media but, as discussed above, is currently limited to video frame rates, i.e.,  $30 \text{ s}^{-1}$  or  $0.034 \text{ s}^{-1}$  while the temperature resolution is dependent upon the heating holder and TEM configuration used, as explained in Section 1.4.

#### *Electron diffraction*

Selected area diffraction patterns, recorded at various temperatures and time intervals (temperature- and time-resolved), are commonly used to identify the onset of reaction and the formation of intermediate phases. Schoen et al. have performed controlled heating experiments to follow the formation of  $\text{CuInSe}_2$  nanowires by solid state diffusion of Cu in  $\alpha\text{-In}_2\text{Se}_3$  nanowires oriented along different directions with respect to the Cu source.[71] Although there was not any appreciable change in structure and morphology, the diffraction patterns changed due to incorporation of Cu into the  $\text{In}_2\text{Se}_3$  lattice and the transformation from the  $\text{In}_2\text{Se}_3$  to the  $\text{CuInSe}_2$  structure. The appearance of streaking in the diffraction patterns along 0001, indicates that the transformation to  $\text{CuInSe}_2$  proceeds through the formation of a disordered intermediate structure at temperatures as low as  $225 \text{ }^\circ\text{C}$  as Cu is incorporated within the  $\text{In}_2\text{Se}_3$  phase (Figure 8a-b). An ordered  $\text{CuInSe}_2$  structure (Figure 8c) that is stable after cooling (Figure 8d) was observed to form upon further heating to  $350 \text{ }^\circ\text{C}$ . Conversely,  $\text{In}_2\text{Se}_3$  nanowires oriented along  $\langle 11\bar{2}0 \rangle$  direction with respect to the Cu source transform directly to the crystalline  $\text{CuInSe}_2$  phase above  $470 \text{ }^\circ\text{C}$ , indicating that Cu diffusion in  $\text{In}_2\text{Se}_3$  is dependent upon the crystallographic orientation. It also shows that the synthesis temperature of nanowires with anisotropic structures can be controlled by their crystallographic orientation.

Other examples of determining structural transformations using electron diffraction include the nitridation reaction of Cu-Cr and Cu-Ti thin films,[50] the initial stages of oxidation of Cu-Au

alloy,[72] the structural phase transition in  $\text{Ca}_2\text{Fe}_2\text{O}_5$ ,[73] microstructural evolution of Ni-Al thin films with temperature,[74] and the electric field induced phase transition in Nb-doped  $\text{Pb}(\text{Zr}_{0.95}\text{Ti}_{0.05})\text{O}_3$ . [47]

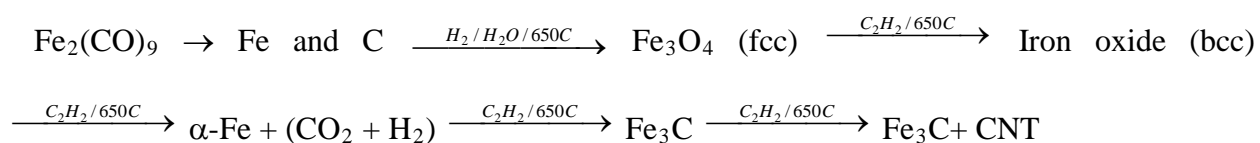
### ***High-resolution imaging***

Time- and temperature-resolved high-resolution imaging is another method to follow structural changes during chemical reaction. The group at the University of Oxford has successfully used an ETEM to determine the structural modifications occurring during oxidation reactions of  $\text{Nb}_{12}\text{O}_{29}$  to  $\text{Nb}_{22}\text{O}_{54}$ . [75] Moreover, they also synthesized a new compound using the chemical and structural information of the defect structure formed during the process. [76]. Temperature-resolved high-resolution imaging has also revealed the appearance and disappearance of an ordered superlattice during temperature cycling from 600 °C to 700 °C for ceria ( $\text{CeO}_2$ ). [77] These structures were formed due to oxygen vacancy ordering in  $\text{CeO}_2$  during reduction in  $\text{H}_2$  at 730 °C and disappeared as the crystal re-oxidized upon cooling to 600 °C. This was a direct observation of the redox behavior of  $\text{CeO}_2$  and a measure of its oxygen storage capacity. [77] Nucleation-and-growth studies of a number of nanostructures such as nanowires and nanotubes have also been reported. High-resolution images have shown that these materials nucleate and grow via vapor-liquid-solid (VLS) or vapor-solid-solid (VSS) mechanism depending upon the chemical system. [29, 30, 62, 63] For example, Si nanowires grow via a VLS mechanism when silane or disilane is introduced in the TEM column over Au catalyst heated above the Au-Si eutectic temperature. On the other hand, they grow via a VSS mechanism below eutectic temperature using the Pd as a catalyst. Whereas Au-Si liquid acts as catalyst in first case, solid  $\text{PdSi}_2$  is the catalyst for the latter. [30]

Carbon nanotubes (CNTs) have also been reported to grow via a VSS mechanism. [59, 66] High-resolution images have recently been used to determine the physical and chemical state of iron-based catalyst particles during carbon nanotube growth. [59, 78] Sharma et al. have also shown the structural transformations occurring in the iron catalyst particles before CNT nucleation and growth. [78] They used the column of an environmental scanning transmission electron microscope (ESTEM) as a flow reactor for both Fe particle and CNT synthesis. First, arrays of equidistant Fe particles were deposited onto a perforated  $\text{SiO}_2$  thin film suspended on a Si wafer support by electron beam induced decomposition (EBID) of nonacarbonyldiiron ( $\text{Fe}_2(\text{CO})_9$ ) vapors at room temperature in the column of the ETEM. *In situ* electron energy-loss spectroscopy (EELS) data confirmed the formation Fe-containing particles and a small amount of carbon. Next, these particles were heated to the reaction temperature (650 °C) in hydrogen to

remove the co-deposited carbon. The hydrogen was then replaced by acetylene, leading to the formation of carbon nanotubes.[39]

Structural transformations in the catalyst particles could be deduced from the diffractograms of individual high resolution images extracted from the video sequence. Fe particles were found to oxidize in the low (0.001 Pa) vacuum of the TEM column to form magnetite (Fe<sub>3</sub>O<sub>4</sub>) upon heating (Figure 9a), but reduce when 0.08 Pa of acetylene at 650 °C was introduced in the sample region. The face centered cubic (fcc) magnetite structure transformed to a body centered cubic (bcc) oxide structure before reducing to ferrite (bcc α-Fe; Figure 9b). In the next stage, the particles are carburized to iron carbide (cementite, Fe<sub>3</sub>C; Figure 9c) before nucleating carbon nanotubes (Figure 9d). Time-resolved high-resolution imaging confirms that the particles remain crystalline throughout these phase transformations. High-resolution images are also used to obtain an atomic-scale understanding of the nucleation of graphene sheets on the Fe-terminated (001) surface of cementite. The following reaction sequence was deduced using high-resolution images recorded as the reactions proceeded:



As catalytic decomposition of hydrocarbons by Fe nanoparticles can either result in the formation of a graphitic layer encapsulating the catalyst, thereby deactivating it, or in the formation of carbon nanotubes. This technique is also relevant for understanding other catalytic reactions.

## 1.5.2 Chemical Changes

While both electron-diffraction patterns and high-resolution images provide information about structural changes, spectroscopic techniques are needed to determine the chemical composition and oxidation state of the reactant, product or intermediate compound. Spectroscopy data can be obtained along with structural information or independently using either X-ray energy-dispersive spectroscopy (XEDS or EDS) or electron energy-loss spectroscopy (EELS). EDS is ill suited for *in situ* studies during the course of a chemical reaction because (a) infrared radiation from the heated specimen tends to swamp the detector at elevated temperatures, and (b) high gas pressures can damage the thin windows in front of the detector. EDS is therefore best suited to obtain chemical information of reactants and products before and after reaction. On the other hand,

EELS is suitable for following the chemical changes during gas-solid interactions, such as reduction, oxidation, nitridation, etc., since the EELS detector is spatially remote from the specimen area and the vast majority of the EELS signal can be collected within a few mrad of the incident beam direction, and is thus not significantly attenuated by the differential pumping apertures of the ETEM.

Spectroscopy techniques can be used to obtain qualitative or quantitative information. For example, EELS was used to determine the presence of N to confirm that the N was incorporated within the nanowires formed after the Au/Ga droplets were exposed to  $\text{NH}_3$  at 800 °C. [79] Moreover, near-edge fine structure for selected elements, such as the  $L_{2,3}$  edges (measuring transitions from 2p to 3d bound states) of third-row transition metals and the  $M_{4,5}$  edges (3d to 4f transition) of the lanthanide family of elements is sensitive to their oxidation state and can be used to follow the changes in it during redox reactions.[80] A shift in the position and/or in the relative intensity of  $L_2$  and  $L_3$  ( $M_4$  and  $M_5$  for lanthenides) of the characteristic edge (also referred as white-lines) is also indicative of a change in oxidation state. The extent of reduction in ceria and doped ceria has been determined quantitatively as described below:

Intrinsic and doped ceria ( $\text{CeO}_2$ ) are often used as catalyst or catalyst support due to their ability to release lattice oxygen (reduction) or to uptake environmental oxygen (oxidation) depending upon the oxygen potential in the ambient environment. In simple terms Ce can co-exist and switch between +3 and +4 oxidation states, and therefore exhibits a property called oxygen storage capacity or OSC.[81] Figure 10a shows the change in the Ce  $M_4$  and  $M_5$  white-line intensities with temperature when heated in  $\approx 260$  Pa of flowing hydrogen.[82] We also know that the oxygen to cerium ratio should change as the material loses oxygen due to reduction that corresponds to  $\text{CeO}_2$  (+4 Ce) converting to  $\text{CeO}_{1.5}$  (+3 Ce). However, these intensity ratios cannot be used directly to quantify the Ce oxidation state as the measurements of the Ce  $M_{4,5}$  cross-sections in the literature differ by a factor of almost two.[83, 84] Moreover, for ceria nanoparticles, surface adsorbents such as water may also contribute to the observed oxygen signal. The change in Ce  $M_5/M_4$  ratio against oxidation states, determined from Ce/O signal, was plotted to obtain the quantitative change in oxidation state with temperature (Figure 10b).[82] These results show that Ce  $M_5/M_4$  ratio can be used to determine the oxidation state and have been successfully employed to follow the redox behavior of individual nanoparticles in mixed cerium-zirconium oxides.[85]

Crozier and Chenna have recently reported a procedure for quantitative measurement of the composition of gas mixtures using EELS. They have shown that valence-loss (or low-loss)

region of EELS data can provide the composition of gas mixture used for understanding the catalytic processes in the ESTEM.

Energy-filtered TEM (EFTEM) imaging, using an in-column or post-column filter, can also be employed to follow the progression of a reaction front. Recently EFTEM has been used to show that a 2 nm amorphous layer of Ni-Si is present in as-deposited samples due to interdiffusion of Ni and Si at room temperature.[86] *In situ* imaging acquired at elevated temperature show an increase in the thickness of this reaction layer as Ni reacts with Si to form nickel silicides, as confirmed by diffraction and imaging.

### 1.5.3 Reaction Rates (Kinetics)

Reaction kinetics at the nanoscale can be quite different from the bulk due to differences in surface area, structure of the bonding planes, *etc.* For example, theoretical calculations have shown that the carbon diffusion rate is different for various crystallographic planes of bcc and fcc iron.[87] *In situ* measurements can provide direct evidence of such subtle differences.

Reaction rates can be measured by following changes in length, diameter, area, volume or chemical composition with time and temperature. The measured rates at various temperatures are then used to calculate the activation energy for the particular reaction using the Arrhenius equation. Baker et al. have done pioneering work for calculating activation energies for CNT formation for different transition metals catalysts.[88] Sinclair's group has used *in situ* measurements extensively for solid-state reactions in microelectronic materials.[89-91] Various examples of measuring reaction kinetics can be found in a recent review paper and the references therein.[39]

## 1.6 LIMITATIONS AND FUTURE DEVELOPMENTS

It is not possible to follow each and every chemical reaction using *in situ* TEM related techniques. Some examples that are beyond the reach of current technology are:

1. Corrosive Gasses: Reactions involving gasses such as NO<sub>x</sub>, SO<sub>x</sub>, H<sub>2</sub>S, and halogens (F, Cl, Br) as reactant or products will corrode the materials currently used in TEM column and holders.
2. Temperature: The design of heating holders and the microscope configuration limit achievable temperatures. For example, although samples can be heated up to 1500 °C using filament heating holders, current differentially pumped TEMs limit the highest attainable temperature to 900 °C when gasses are introduced in the sample chamber.

Other issues with currently available commercial heating holders pertain to a relative lack

of control over heating and cooling rates and thermal drift that make it difficult to collect good quality data. For example, samples continue to drift due to expansion of various components for 15 min to 20 min after reaching the desired observation temperature. Therefore, high-resolution images or nanoscale spectroscopy cannot be recorded during this period, making it quite difficult to obtain temperature resolved data. Some new commercial designs to overcome some of these difficulties have been reported recently.[13]

3. **Temporal Resolution:** Observable reaction rates are dependent upon our recording method. Therefore, any reaction occurring faster than the recording rate cannot be captured. Currently this limit for video imaging is  $\sim 1/30$  s and for EDS is  $\sim 20$  s. However, there are some recent developments that may help in overcoming this limitation. For example, Kim et al. have recently reported the ability to capture data for faster reaction rate processes by combining pulsed heating with pulsed electron beam imaging or diffraction.[70] Post-column EELS detectors capable of recording 100 energy-loss spectra in one second have recently been introduced, but the feasibility for obtaining data with good signal-to-noise ratios for nanoparticles is not yet certain. It is worth noting that *in situ* measurements are not only limited in their ability to follow fast reactions, but are also not suited for following reaction processes that take weeks or months, such as the effect of thermal cycles on materials used in solid oxide fuel cells or the processes leading to the deactivation of catalysts after multiple cycles.

## 1.7 ACKNOWLEDGEMENTS

Stimulating discussions and scientific contributions from Professors Peter Crozier, Maria Gajdarziska, Michael Treacy, and Peter Rez, Doctors Ruigang Wang and See Wee Chee, and Michael McKelvy are gratefully acknowledged. Mr. Karl Wise has been an integral part of ASU's ETEM group. Funding from NSF and DOE for the ETEM purchase, modifications and various research projects is also gratefully acknowledged. The author is also grateful to Andrew Berglund, J. Alexander Liddle, Mark Stiles and Ian M. Anderson of NIST for their review and comments for improving this manuscript.

## 1.8 REFERENCES

1. Sharma, R., and Weiss, K., *Development of a TEM to study in situ structural and chemical changes at atomic level during gas solid interaction at elevated temperatures*. Microscopy Research & Technique, 1998. **42**(4): p. 270-280.
2. Daulton, T.L., Little, B.J., Lowe, K., Jones-Meehan J., *In situ environmental cell-transmission electron microscopy study of microbial reduction of chromium (VI) using electron energy loss spectroscopy*. Microscopy and Microanalysis, 2001. **7**: p. 470.
3. Doole, R.C., Parkinson, G.M., and Stead, J.M., *High Resolution Gas Reaction Cell for the JEM 4000*. Institute of Physics Conference Series, 1991. **119**: p. 157-160.
4. Swann, P.R., and Tighe, N.J. *Performance of differentially pumped environmental cell in the AEI EM7*. in *Proc. 5th Eur. Reg. Cong Electron Microscopy*. 1972.
5. Parkinson, G.M., *High resolution, in-situ controlled atmosphere transmission electron microscopy (CTEM) of heterogeneous catalysts*. Catalysis Letters, 1989. **2**: p. 303-307.
6. Parkinson, G.M., *Controlled environment transmission electron microscopy (CTEM) of catalysis*. Institute of Physics Conference Series, 1991. **119**: p. 151-156.
7. Robertson, I.M., Teter, D., *Controlled Environment Transmission Electron Microscopy*. Microscopy Research & Technique, 1998. **42**(4): p. 260-269.
8. Gai, P.L., *Development of wet environmental TEM (Wet-ETEM) for in situ studies of liquid-catalyst reactions on the nanoscale*. Microscopy and Microanalysis, 2002. **8**: p. 21.
9. Kamino, T., Saka, H., *Newly developed high resolution hot stage and its applications to materials science* Microscopy, Microanalysis and Microstructure, 1993. **4**: p. 127-135.
10. Kamino, T., Yaguchi, T., Konno, M., Watabe, A., Marukawa, T., Mima, T., Kuroda, K., Saka, H., Arai, S., Makino, H., Suzuki Y., and Kishita K., *Development of a gas injection/ specimen heating holder for use with transmission electron microscope*. Journal of Electron Microscopy, 2005. **54**(6): p. 497-503.
11. Creemer, J.F., et al., *Atomic-scale electron microscopy at ambient pressure*. Ultramicroscopy, 2008. **108**(9): p. 993-998.
12. Takeo, K., et al., *Development of a specimen heating holder with an evaporator and gas injector and its application for catalyst*. Journal of Electron Microscopy, 2006. **55**(5): p. 245-252.
13. Allard, L.F., et al., *A New MEMS-Based System for Ultra-High-Resolution Imaging at Elevated Temperatures*. Microscopy Research and Technique, 2009. **72**(3): p. 208-215.
14. Tan, X., Xu, Z., Shang, JK, Han, P., *Direct observations of electric field-induced domain boundary cracking in <001> oriented piezo-electric  $Pb(Mg_{1/3}Nb_{2/3})O_3$ - $PbTiO_3$  single crystal*. Applied Physics Letters, 2000. **77**: p. 1529-1531.
15. Qu, W., , Zhao, X., Tan, X., *Evolution of nanodomains during the electric field-induced relaxor to normal phase transition in a Sc-doped  $Pb(Mg_{1/3}Nb_{2/3})O_3$  ceramic* Journal of Applied Physics, 2007. **102**: p. 084101 (1-8).
16. Williamson, M.J., Tromp, R.M., Vereecken, P.M., Hull, R., and Ross, F.M., *Dynamic microscopy of nanoscale cluster growth at the solid-liquid interface*. Nature Materials, 2003. **2**: p. 532-536.
17. Ross, F.M. and P.C. Searson. *Dynamic observation of electrochemical etching in silicon*. 1995: Iop Publishing Ltd.
18. Zheng, H.M., et al., *Observation of Single Colloidal Platinum Nanocrystal Growth Trajectories*. Science, 2009. **324**(5932): p. 1309-1312.
19. Zheng, H.M., et al., *Nanocrystal Diffusion in a Liquid Thin Film Observed by in Situ Transmission Electron Microscopy*. Nano Letters, 2009. **9**(6): p. 2460-2465.
20. Daulton, T.L.L., B.J. Lowe, K. and Jones-Meehan J., *In situ environmental cell-transmission electron microscopy study of microbial reduction of chromium (VI) using electron energy loss spectroscopy*. Microscopy and Microanalysis 2001. **7**: p. 470.

21. Sakai, N., Xiong, Y.P., Yamaji, K., Kishimoto, H., Horita, T., Brito, M.E., Yokokawa, H., *Transport properties of ceria-zirconia-ytria solid solutions*  $\{(CeO_2)_x(ZrO_2)_{1-x}\}_{1-y}(YO_{1.5})_y$  ( $x = 0-1$ ,  $y = 0.2, 0.35$ ). *Journal of Alloys and Compounds*, 2006. **408-412**: p. 503-506.
22. Chen, C.L. and H. Mori, *In situ TEM observation of the growth and decomposition of monoclinic W18O49 nanowires*. *Nanotechnology*, 2009. **20**(28): p. 6.
23. Sharma, R., *An environmental transmission electron microscope for in situ synthesis and characterization of nanomaterials*. *Journal of Materials Research*, 2005. **20**(7): p. 1695-1707.
24. Kammler, M., et al., *Lateral control of self-assembled island nucleation by focused-ion-beam micropatterning*. *Applied Physics Letters*, 2003. **82**(7): p. 1093-1095.
25. Lang, C., et al., *Real time observation of GeSi/Si(001) island shrinkage due to surface alloying during Si capping*. *Physical Review Letters*, 2006. **97**(22): p. 4.
26. Portavoce, A., et al., *Mechanism of the nanoscale localization of Ge quantum dot nucleation on focused ion beam templated Si(001) surfaces*. *Nanotechnology*, 2006. **17**(17): p. 4451-4455.
27. Kim, B.J., et al., *Determination of Size Effects during the Phase Transition of a Nanoscale Au-Si Eutectic*. *Physical Review Letters*, 2009. **103**(15): p. 4.
28. Dick, K.A., et al., *Control of GaP and GaAs Nanowire Morphology through Particle and Substrate Chemical Modification*. *Nano Letters*, 2008. **8**(11): p. 4087-4091.
29. Kim, B.J., et al., *Kinetics of Individual Nucleation Events Observed in Nanoscale Vapor-Liquid-Solid Growth*. *Science*, 2008. **322**(5904): p. 1070-1073.
30. Hofmann, S., Sharma, R., Wirth, C.T., Cervantes-Sodi, F., Ducati, C., Kasama, T., R. E. Dunin-Borkowski, Drucker, J., Bennet, P., Robertson, J., *Ledge-flow controlled catalyst interface dynamics during Si nanowire growth*. *Nature Materials*, 2008. **7**(5): p. 372-375.
31. Yeadon, M., et al., *In situ transmission electron microscopy of AlN growth by nitridation of (0001)alpha-Al2O3*. *Journal of Applied Physics*, 1998. **83**(5): p. 2847-2850.
32. Lin, M., Tan, Joyce Pei Ying, Boothroyd, Chris, Loh, Kian Ping, Tok, Eng Soon, and Foo, Yong-Lim *Dynamical Observation of Bamboo-like Carbon Nanotube Growth*. *Nano Letters*, 2007. **7**(8): p. 2234-2238.
33. Birnbaum, H.K., and Sofronis, P., *Hydrogen enhanced local plasticity - a mechanism for hydrogen-related fracture*. *Materials Science and Engineering*, 1993. **A176**: p. 191
34. Gai, P.L., *Environmental high resolution electron microscopy of gas-catalyst reactions*. *Topics in Catalysis*, 1999 **8**: p. 97-113.
35. Hansen, T.W., Wagner, J.B., Hansen, P.L., Dahl, S., Topsoe, H., and Jacobsen, J.H., *Atomic-resolution in situ transmission electron microscopy of a promoter of a heterogeneous catalyst*. *Science*, 2001. **294**: p. 1508-1510.
36. Sharma, R., Crozier, Peter A., *Environmental Transmission Electron Microscopy in Nanotechnology*, in *Transmission Electron microscopy for nanotechnology*, N.Y.Z.L. Wang, Editor. 2005, Springer-Verlag and Tsinghua University Press. p. 531-565.
37. Gai, P.L., R. Sharma, and F.M. Ross, *Environmental (S)TEM studies of gas-liquid-solid interactions under reaction conditions*. *Mrs Bulletin*, 2008. **33**(2): p. 107-114.
38. Sharma, R., *Observation of Dynamic Processes using Environmental Transmission and Scanning Transmission Electron Microscope*, in *In Situ Electron Microscopy at High Resolution*, F. Banhart, Editor. 2008, World Scientific Publishing Ltd.
39. Sharma, R., *Kinetic Measurements From In Situ TEM Observations*. *Microscopy Research and Technique*, 2009. **72**(3): p. 144-152.
40. Stach, E.A., *Real-time observations with electron microscopy*. *Materials Today*, 2008. **11**: p. 50-58.
41. Fornasiero, P., Di Monte, R., Ranga Rao, G., Kaspar, J., Meriani, S., Trovarelli, A., Graziani, M., *Rh-loaded CeO<sub>2</sub>-ZrO<sub>2</sub> solid solutions as highly efficient oxygen*

- exchangers: dependence of the reduction behavior and the oxygen storage capacity on the structural properties.* Journal of Catalysis, 1995 **151**: p. 168-177.
42. Fornasiero, P., Balducci, G., Kaspar, J., Meriani, S., Di Monte, R., Graziani, M., *Metal-loaded CeO<sub>2</sub>-ZrO<sub>2</sub> solid solutions as innovative catalysts for automotive catalytic converters.* Catalysis Today, 1996. **29**: p. 47-52.
  43. Ruigang Wang, P.A.C., Renu Sharma, James B. Adams, *Nanoscale heterogeneity in ceria zirconia with low temperature redox properties.* Journal of Physical Chemistry B, 2006. **110**: p. 18278-18285.
  44. Naik, V.M., Haddad, D., Naik, R., Benci, J., Auner, G.W. *Solid-State Chemistry of Inorganic Materials IV.* in *Materials Research Society Symposium Proceedings*. 2002. 755: p. 413-417.
  45. de Graaf, M., Willard, M.A., McHenry, M.E., Zhu, Y.M., *In-situ Lorentz TEM coolong study of magnetic domain configuration in Ni<sub>2</sub>MnGa.* IEEE Transactions on Magnetics, 2001. **37**(4): p. 2663-2665.
  46. Tsuchiya, K., Yamamoto, K., Hirayama, T., Nakayama, H., Todaka, Y., Umemoto, M. *TEM observation of phase transformation and magnetic structure in ferromagnetic shape memory alloys.* in *Electron microscopy: its role in Materials Science-The Mike Meshii Symposium*. 2003.
  47. Qu, W.G., X.L. Tan, and P. Yang, *In Situ Transmission Electron Microscopy Study on Nb-Doped Pb(Zr0.95Ti0.05)O-3 Ceramics.* Microscopy Research and Technique, 2009. **72**(3): p. 216-222.
  48. Oleshko, V.P., Crozier, P.A., Cantrell, R.D., Westwood, A.D., *In-situ and ex-situ study of gas phase propylene polymerization over a high activity TiCl<sub>4</sub>-MgCl<sub>2</sub> heterogeneous zeigler-natta catalyst* Macromol. Rapid Commun., 2001. **22**: p. 34-40.
  49. Oleshko, V.P., Crozier, P.A., Cantrell, R.D., Westwood, A.D., *In-situ real-time environmental TEM of gas phase ziegler-natta catalytic polymerization of propylene.* Journal of Electron Microscopy, 2002. **51** (Suppl.): p. S27-39.
  50. Atzmon, Z., Sharma, R., Mayer, J.W., and Hong, S.Q., *An in situ transmission electron microscopy study during NH<sub>3</sub> ambient annealing of Cu-Cr thin Films.* Proceedings of Materials Research Society Symposium, 1993. **317**: p. 245-250.
  51. Atzmon, Z., Sharma, R. Russell, S.W., and Mayer, J.W., *Kinetics of copper grain growth during nitridation of Cu-Cr and Cu-Ti thin films by in situ TEM.* Proceedings of Materials Research Society Symposium, 1994. **337** p. 619-624.
  52. Sharma, R., McKelvy, Michael J., Béarat, Hamdallah, Chizmeshya, Andrew V.G., and Carpenter, R.W., *In Situ Nanoscale Observations of the Mg(OH)<sub>2</sub> Dehydroxylation and Rehydroxylation Mechanisms.* Philosophical Magazine, 2004. **84**: p. 2711-2729.
  53. McKelvy, M.J., Sharma, Renu, Chizmeshya, Andrew V.G., Carpenter, R.W., Streib, Ken *Magnesium Hydroxide Dehydroxylation: In situ nanoscale observations of lamellar nucleation and growth.* Chemistry of Materials, 2001. **13**(3): p. 921-926.
  54. Gajdardziska-Josifovska, M. and R. Sharma, *Interaction of oxide surfaces with water: Environmental transmission electron microscopy of MgO hydroxylation.* Microscopy and Microanalysis, 2005. **11**(6): p. 524-533.
  55. Freney, E.J., S.T. Martin, and P.R. Buseck, *Deliquescence and Efflorescence of Potassium Salts Relevant to Biomass-Burning Aerosol Particles.* Aerosol Science and Technology, 2009. **43**(8): p. 799-807.
  56. Wise, M.E., et al., *Water uptake by NaCl particles prior to deliquescence and the phase rule.* Aerosol Science and Technology, 2008. **42**(4): p. 281-294.
  57. Wise, M.E., Biskos, G., Martin, S.T., Russell, L.M., and Buseck, P.R., *Phase transitions of single salt particles studied using a transmission electron microscope with an environmental cell.* Aerosol Science and Technology, 2005. **39**: p. 849-856.

58. Semeniuk, T.A., Wise, Matthew E., Martin, Scot T., Russell, Lynn M., Buseck, Peter R. , *Hygroscopic behavior of aerosol particles from biomass fires using environmental transmission electron microscopy*. Journal of Atmospheric Chemistry, 2007. **56**(3): p. 259-273.
59. Yoshida, H., Takeda, Seiji, Uchiyama, Tetsuya, Kohno, Hideo, Homma, Yoshikazu, *Atomic-Scale In-situ Observation of Carbon Nanotube Growth from Solid State Iron Carbide Nanoparticles*. Nano Letters, 2008. **9**(11): p. 3810-3815.
60. Terrones, M., et al., *Nanotubes: A revolution in materials science and electronics*, in *Fullerenes and Related Structures*. 1999, Springer-Verlag Berlin: Berlin. p. 189-234.
61. Silvis-Cividjian, N., Hagen, C. W., Kruit, P., Stam, M. A. J. v.d., Groen, H. B. , *Direct fabrication of nanowires in an electron microscope*. Applied Physics Letters, 2003. **82**(20): p. 3514-3416.
62. Kodambaka, S., Hannon, J.B., Tromp, R.M., and Ross, F.R., *Control of Si nanowire growth by oxygen*. Nano Letters, 2006. **6**(6): p. 1292-1296.
63. Kodambaka, S., et al., *Germanium nanowire growth below the eutectic temperature*. Science, 2007. **316**(5825): p. 729-732.
64. Sharma, R., Zafar, Iqbal *In situ observations of carbon nanotube formation using environmental electron microscopy (ETEM)*. Applied Physics Letters, 2004. **84**: p. 990-992.
65. Hofmann, S., Sharma, R., Ducati, C., Du, G., Mattevi, C., Cepek, C., Mirco, C., Pisana, S., Parvez, A., Cervantes-Sodi, F., Ferrari, A. C., Dunin-Borkowski, R., Lizzit, S., Petaccia, L., Goldoni, A., Robertson, J., *In situ Observations of Catalyst Dynamics during Surface-Bound Carbon Nanotube Nucleation*. Nano Letters, 2007. **7**(3): p. 602-608.
66. Helveg, S., Lopez-Cartes, C., Sehested, J., Hansen, P.L., Clausen, B.S., Rostrup-Nielsen, J.R., Abild-Pedersen, F., and Norskov J., *Atomic-scale imaging of carbon nanofibre growth*. Nature, 2004. **427**: p. 426
67. Mima, T., et al., *In situ transmission electron microscopy observation of the growth of bismuth oxide whiskers*. Microscopy and Microanalysis, 2008. **14**(3): p. 267-273.
68. Alani, R. and M. Pan. *In situ transmission electron microscopy studies and real-time digital imaging*. 2001: Blackwell Science Ltd.
69. King, W.E., Campbell, G.H., Frank, A., Reed, B., Schmerge, J.F., Siwick, B.J., and B.C. Stuart, Weber, P.M., *Ultrafast electron microscopy in materials science, biology, and chemistry*. Journal of Applied Physics, 2005. **97**: p. 111101.
70. Kim, J.S., et al., *Imaging of transient structures using nanosecond in situ TEM*. Science, 2008. **321**(5895): p. 1472-1475.
71. Schoen, D.T., H.L. Peng, and Y. Cui, *Anisotropy of Chemical Transformation from In<sub>2</sub>Se<sub>3</sub> to CuInSe<sub>2</sub> Nanowires through Solid State Reaction*. Journal of the American Chemical Society, 2009. **131**(23): p. 7973-+.
72. Wang, L., Zhou, GW, Eastman, J. A., Yang J. C., *Initial oxidation kinetics and energetics of Cu<sub>0.5</sub>Au<sub>0.5</sub> (001) film investigated by in situ ultrahigh vacuum transmission electron microscopy*. Surface Science, 2006. **600**(11): p. 2372-2378.
73. Kruger, H., et al., *High-temperature structural phase transition in Ca<sub>2</sub>Fe<sub>2</sub>O<sub>5</sub> studied by in-situ X-ray diffraction and transmission electron microscopy*. Journal of Solid State Chemistry, 2009. **182**(6): p. 1515-1523.
74. Li, P.Y., et al., *An in-situ TEM investigation on microstructure evolution of Ni-25 at.% Al thin films*. Journal of Alloys and Compounds, 2009. **478**(1-2): p. 240-245.
75. Sayagués, M.J., and Hutchison, J.L. , *From Nb<sub>12</sub>O<sub>29</sub> to Nb<sub>22</sub>O<sub>54</sub> in a controlled environment high resolution microscope*. Journal of Solid State Chemistry, 1999. **146**: p. 202-

76. Sayagués, M.J., and Hutchison, J.L. , *A new niobium tungsten oxide as a result of an in situ reaction in a gas reaction cell microscope*. Journal of Solid State Chemistry, 1999. **143**: p. 33
77. Crozier, P.A., R.G. Wang, and R. Sharma, *In situ environmental TEM studies of dynamic changes in cerium-based oxides nanoparticles during redox processes*. Ultramicroscopy, 2008. **108**(11): p. 1432-1440.
78. Sharma, R., Moore, E.S., Rez, P, Treacy M.M.J., *Site-specific fabrication of Fe particles for carbon nanotube growth*. Nano Letters, 2009. **9**(2): p. 689-694.
79. Diaz, R.E., Sharma, R., Jarvis, K., Mahajan, S. , *Direct observation of nucleation and early stages of growth of GaN nanowires*. Nano Letters, 2010: p. in press.
80. Chueh, Y.L., et al., *Systematic study of the growth of aligned arrays of alpha-Fe<sub>2</sub>O<sub>3</sub> and Fe<sub>3</sub>O<sub>4</sub> nanowires by a vapor-solid process*. Advanced Functional Materials, 2006. **16**(17): p. 2243-2251.
81. Logan, A.D., Shelf, M. , *Oxygen availability in mixed cerium/praeseodymium oxidized and the effect of nobel-metals*. Journal of Materials Research, 1994. **9**(2): p. 468-475.
82. Sharma, R., Crozier, Peter A., Kang Z.C., and Eyring, L., *Observation of dynamic nanostructural and nanochemical changes in Ceria-based catalysts during in situ reduction*. Philosophical Magazine, 2004. **84**: p. 2731-2747.
83. Hofer, F., Golob, P., Brunegger, A., *EEELS quantification of the elements Sr to W by means of M<sub>4,5</sub> Edges*. Ultramicroscopy, 1988. **25**(1): p. 81-84.
84. Manoubi, T., and Colliex, C., *Quantitative Electron Energy Loss Spectroscopy on M<sub>45</sub> Edges in Rare Earth Oxides*. Journal of Electron Spectroscopy and Related Phenomena, 1990. **50**(1): p. 1-18.
85. Wang, R., Crozier, Peter A., Sharma, Renu, and Adams, James B., *Nanoscale heterogeneity in ceria zirconia with low temperature redox properties*. Journal of Physical Chemistry, 2006. **B110**(37): p. 18278-18285.
86. Alberti, A., et al., *Low temperature formation and evolution of a 10 nm amorphous Ni-Si layer on [001] silicon studied by in situ transmission electron microscopy*. Journal of Applied Physics, 2009. **105**(9).
87. Jiang, D.E. and E.A. Carter, *Carbon dissolution and diffusion in ferrite and austenite from first principles*. Physical Review B, 2003. **67**(21).
88. Baker, R.T.K., Harris, P.S., Thomas, R.B., Waite, R.J., *Formation of filamentous carbon from iron, cobalt and chromium catalyzed decomposition of acetylene* Journal of Catalysis, 1973. **30**: p. 86-95.
89. Sinclair, R., M.A. Parker, and K.B. Kim, *INSITU HIGH-RESOLUTION ELECTRON-MICROSCOPY REACTIONS IN SEMICONDUCTORS*. Ultramicroscopy, 1987. **23**(3-4): p. 383-395.
90. Sinclair, R., Min, KH, Kwon, U., *Applications of in situ HREM to study crystallization in materials*. Current Research in Advanced Materials and Processes, 2005. **494**: p. 7-11.
91. MIN, K.-H., SINCLAIR, R., PARK, I.-S., KIM, S.-T., CHUNG, U.-I. , *Crystallization behavior of ALD-Ta<sub>2</sub>O<sub>5</sub> thin films: the application of in-situ TEM*. Philosophical Magazine, 2005. **85**(18): p. 2049-2063.

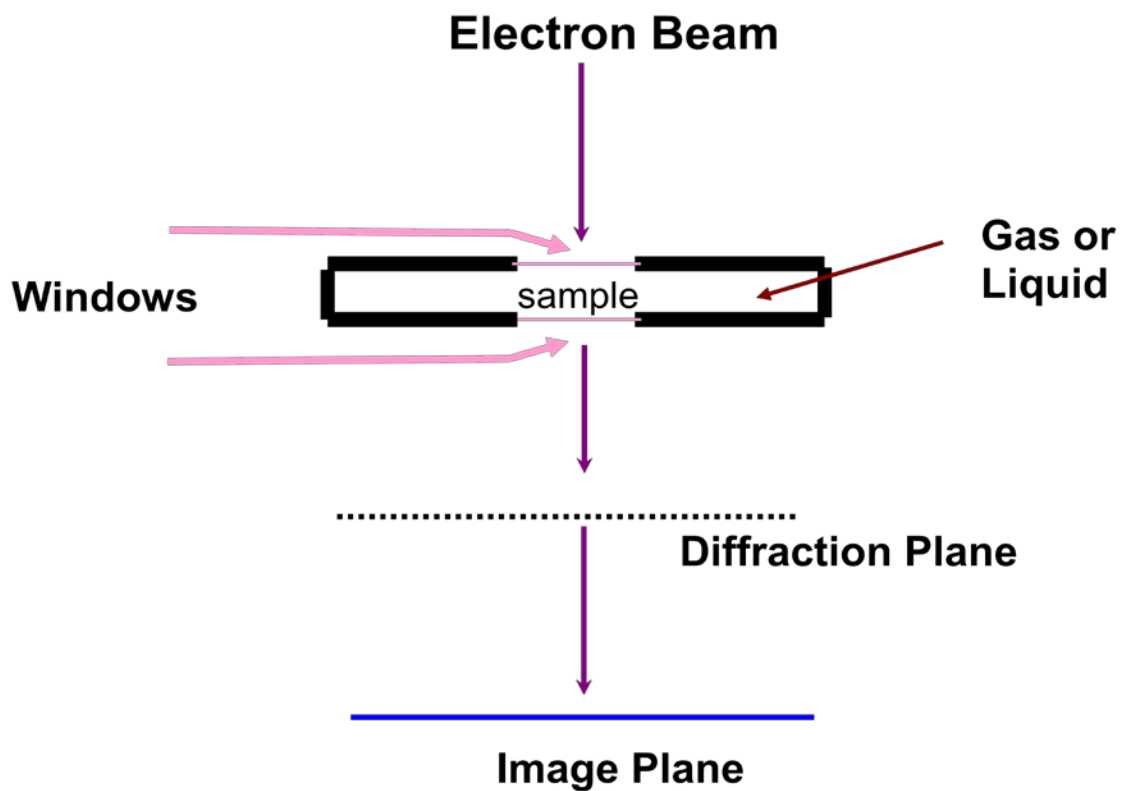


Figure 1. General principle of using electron transparent windows to keep the gas or liquid confined to the area around sample. The electron beam is transmitted through the windows, and interaction with the liquid/gas and solid samples form a diffraction pattern at the diffraction plane and images on the image plane as in a regular TEM.



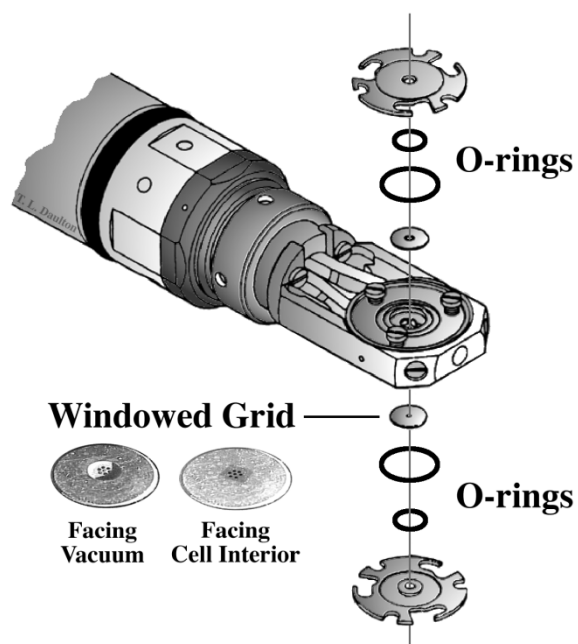


Figure 2. Schematic representation of a commercially available windowed holders consisting of two window grids (above and below the samples), O-rings for sealing, top and bottom screw-fittings to keep the assembly in place. (From Daulton et al., *Microsc. Microanal.* 7 (2001) 470.)

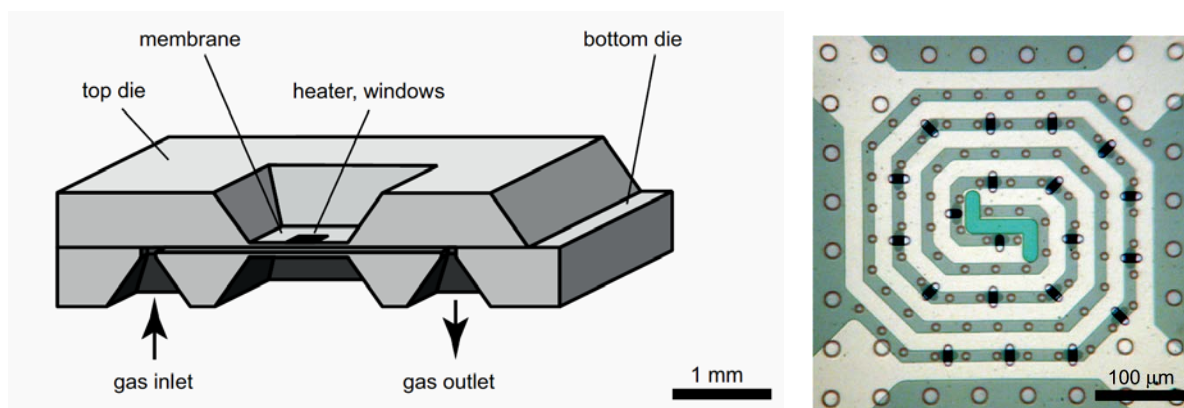
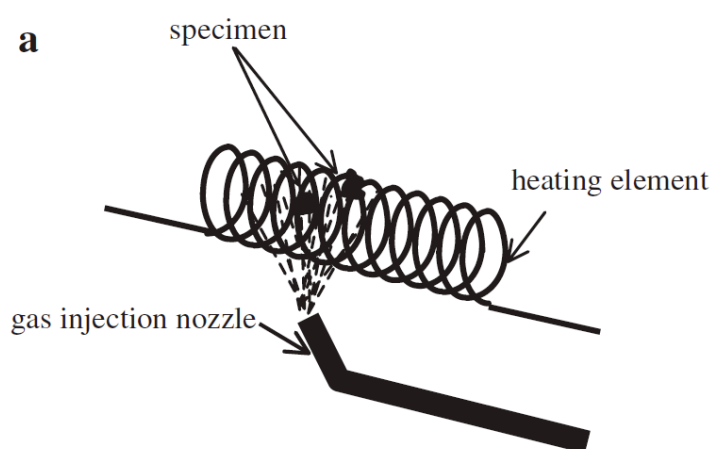


Figure 3. (a) Schematic cross-section of the nanoreactor showing micron sized holes for gas inlet and outlet. (b) Optical close-up of the nanoreactor membrane. The bright spiral is the Pt heater. The small ellipses are the electron-transparent windows. The circles are the SiO<sub>2</sub> spacers that define the minimum height of the gas channel. (After Creemer et al., *Ultramicrosc.* 108 (2008) 993.)



**b**

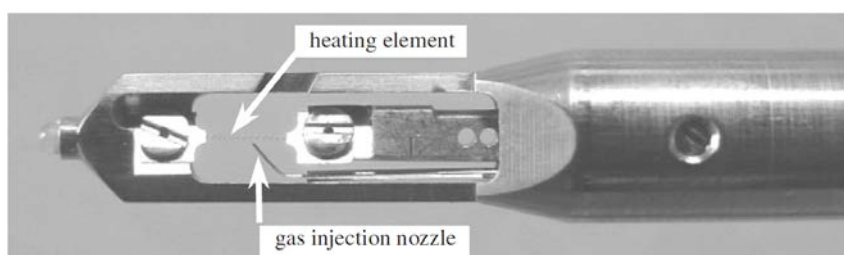


Figure 4. (a) Schematic diagram showing the location of the gas-injector with respect to the heating coil on which a powder sample is loaded. (b) An optical image of the gas injection/specimen heating holder. (From Kamino et al., J. Electron. Microsc. 54 (2005) 497.)

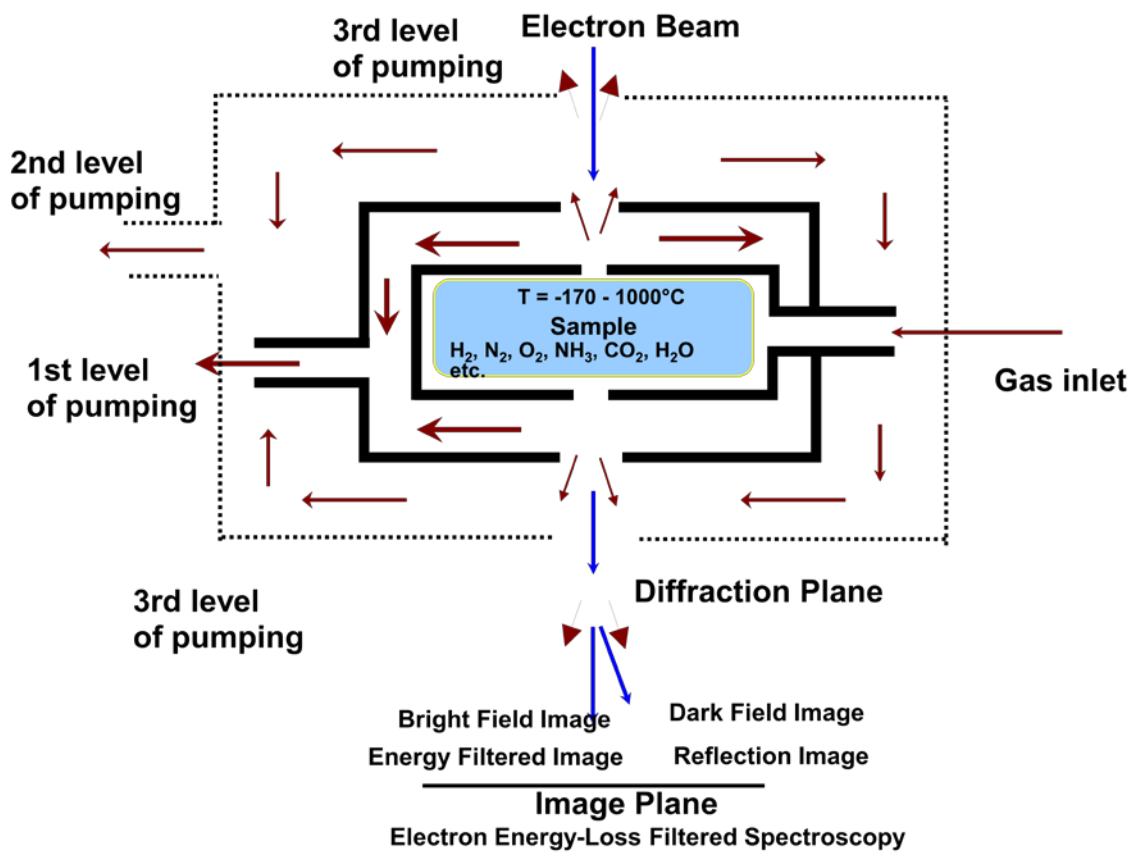


Figure 5. Schematic flow-chart of a three-stage differential pumping system that is used to convert a TEM to an ETEM. Gas is introduced in the sample area and the leak rate into the microscope column is restricted by a set of small apertures (approximately 100  $\mu\text{m}$  diameter), placed above and below the sample. Gas leaked through these apertures is pumped using a magnetically levitated turbo-molecular pump (TMP; 1st level of pumping). The space between the condenser aperture and viewing chamber is pumped using another TMP (2nd level of pumping). The region between condenser aperture and gun chamber is pumped by an ion pump (3rd level of pumping).

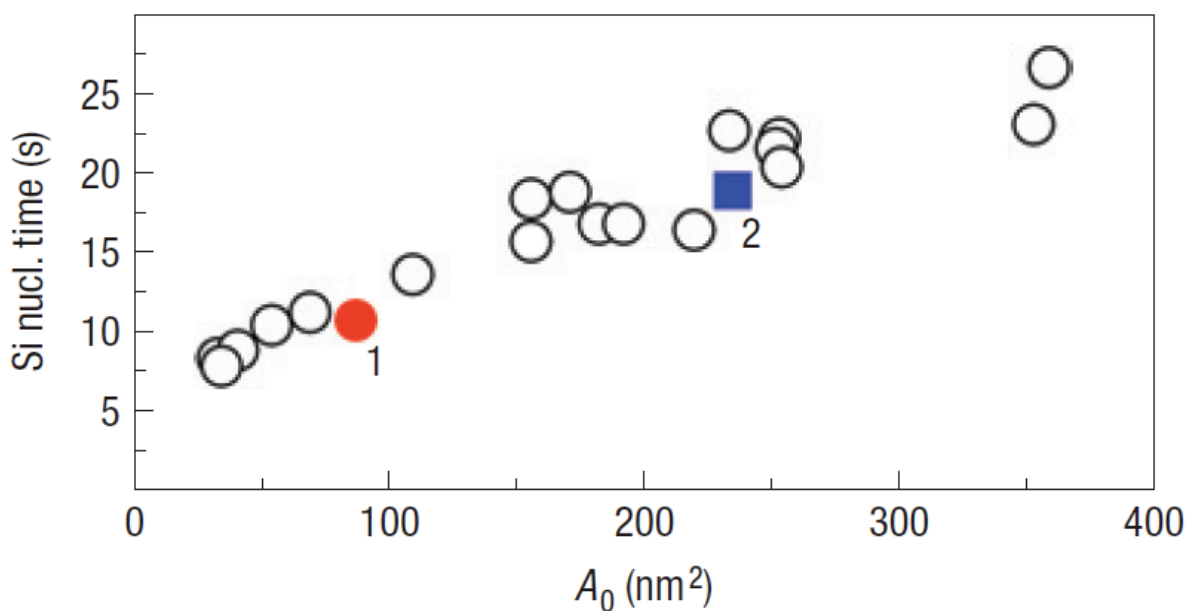
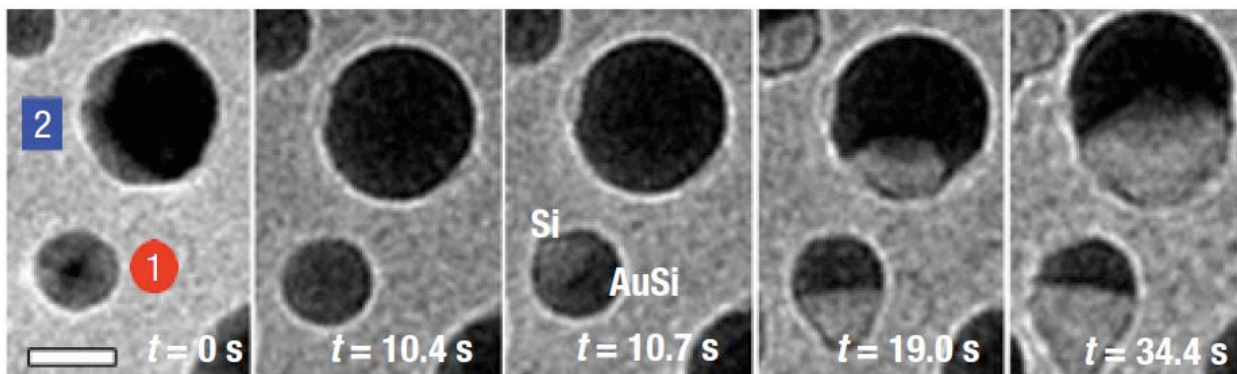


Figure 6. An ETEM image sequence of Au nanoparticles supported on  $\text{SiO}_x$  during exposure to  $\approx 0.13$  Pa of  $\text{Si}_2\text{H}_6$  at  $590^\circ\text{C}$  (scale bar 10 nm), extracted from a video. Time elapsed between images with  $t = 0$  s roughly equal to the onset of disilane exposure is marked on individual images. Note that the nucleation onset (incubation) times for particles 1 and 2 are different. (b) Incubation time for Si precipitation versus  $A_0$ , the cross-sectional area of the initial Au crystal with data points for particles 1 and 2 marked in red and blue respectively. (From Hoffman et al., *Nature Mater.* 7 (2008) 372.)

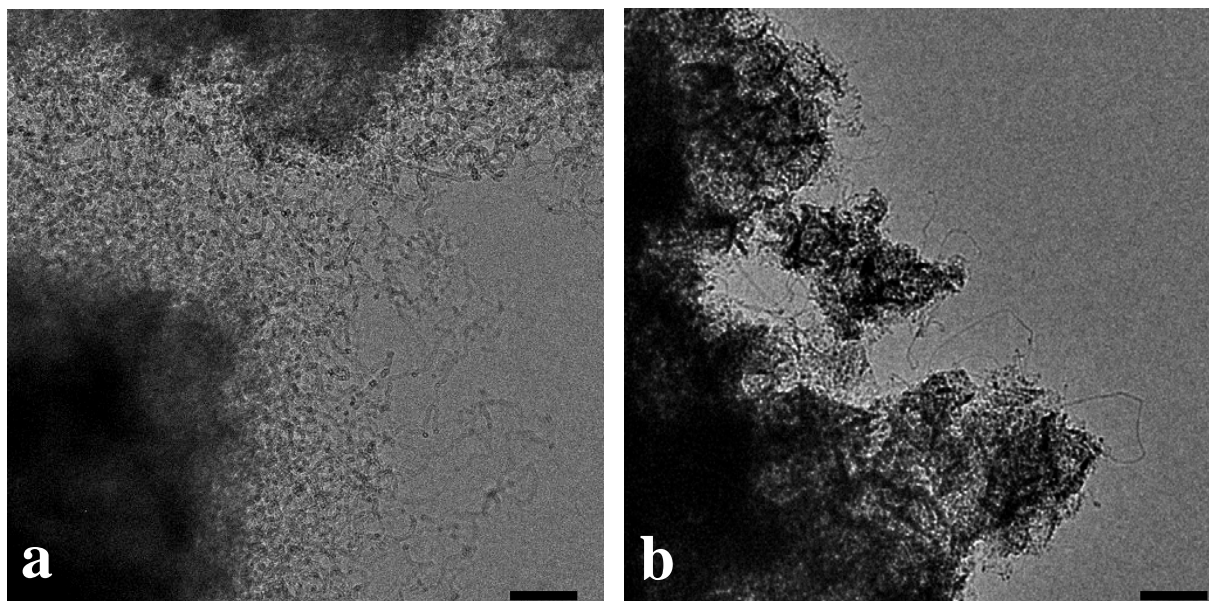
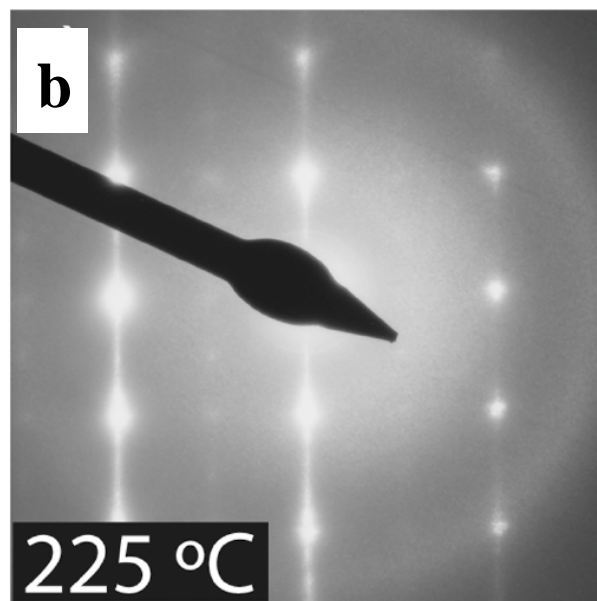
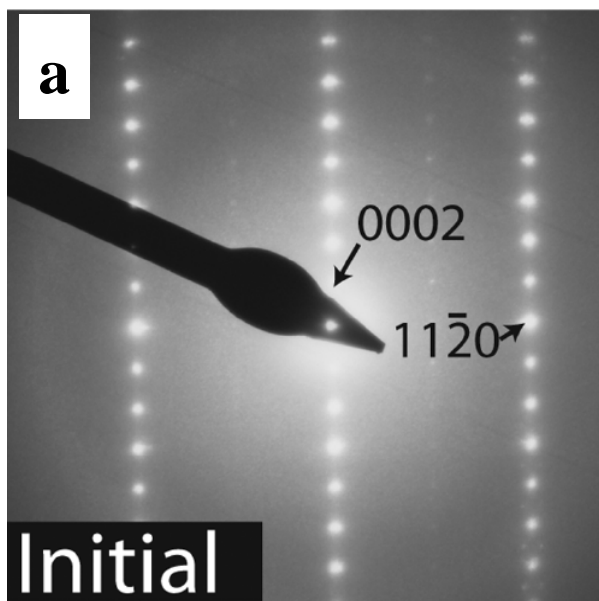
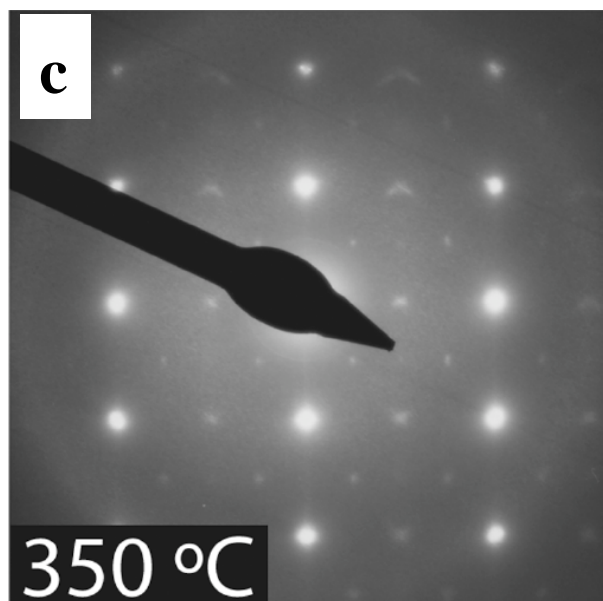


Figure 7. Low magnification images recorded after CNT growth, using ESTEM, when a Ni/SiO<sub>2</sub> sample was dry loaded onto a (a) Au, and (b) Ni support grid under otherwise identical conditions. Note the increased yield of CNTs formed on the Au grid. Bar is 100 nm.





**d**

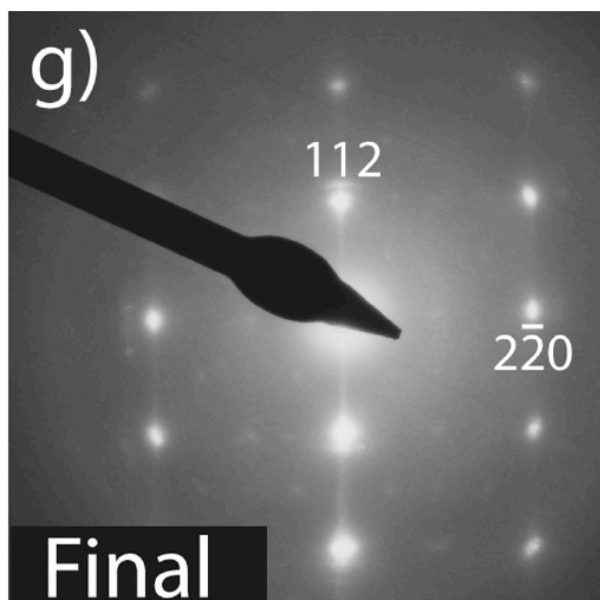


Figure 8. Selected area electron diffraction patterns of an  $\text{In}_2\text{Se}_3$  nanowire with Cu contacts, acquired during *in situ* heating to 350 °C. (a) Prior to heating, the pattern indicates a hexagonal structure with a well defined superstructure normal to the basal planes (0001). (b) The streaking along 0001 at 225 °C indicates the start of Cu diffusion in this plane. (c) A defect-free  $\text{CuInSe}_2$  nanowire with a cubic structure formed upon further heating to 350 °C. (d) The cubic structure was stable upon cooling to room temperature. (From Schoen et al., J. Am. Chem. Soc. 131 (2009) 7973.)

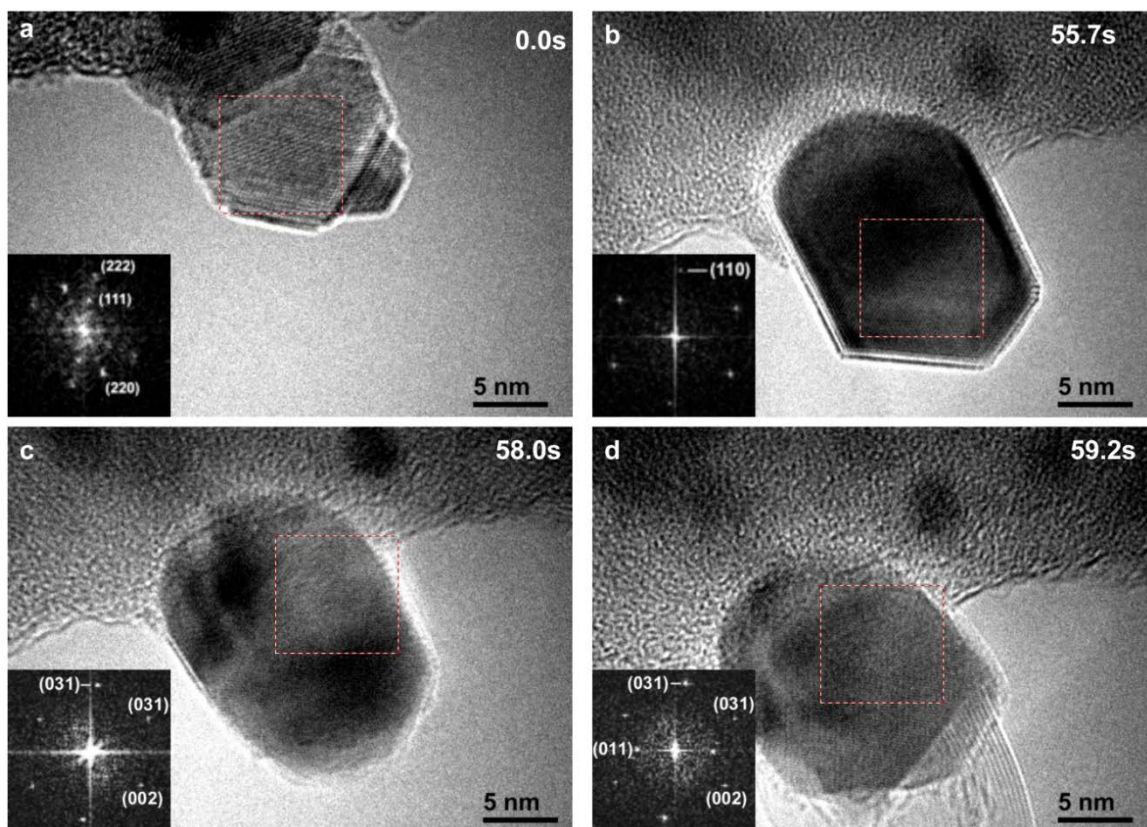


Figure 9. Time-resolved high-resolution images extracted from a digital video recorded at 650 °C in  $\approx 1.33$  Pa ( $10^{-2}$  Torr) of flowing acetylene ( $C_2H_2$ ). Fe-containing catalyst particles were deposited *in situ* by electron beam induced decomposition of  $Fe_2(CO)_9$  vapor. Fast Fourier Transforms (FFTs), or diffractograms, of the area of the particle indicated by the square selection in each frame are shown in the lower left-hand corner; the elapsed time is shown in the upper right hand corner. Diffractograms could be indexed (marked on diffractograms) as (a)  $Fe_3O_4$ , (b)  $\alpha$ -Fe, (c-d)  $Fe_3C$ . The iron carbide phase persists after CNT formation. (From Sharma et al, Nano Lett. 7 (2009))

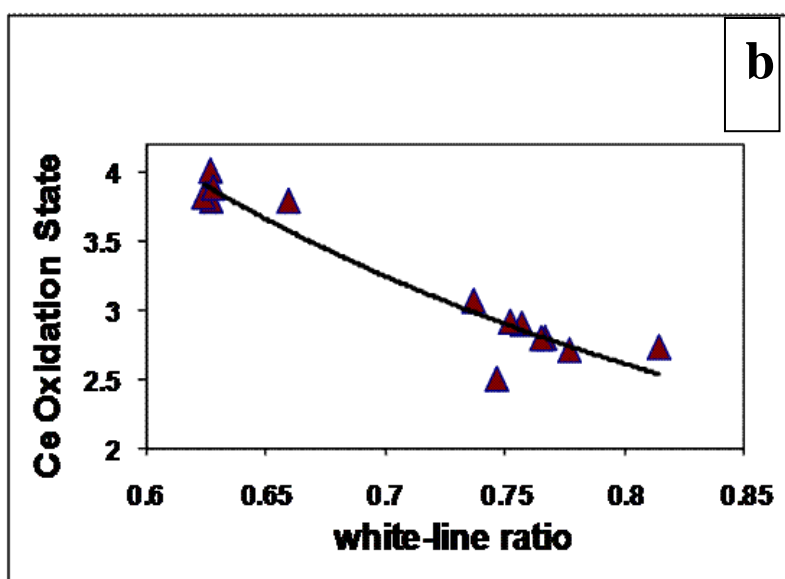
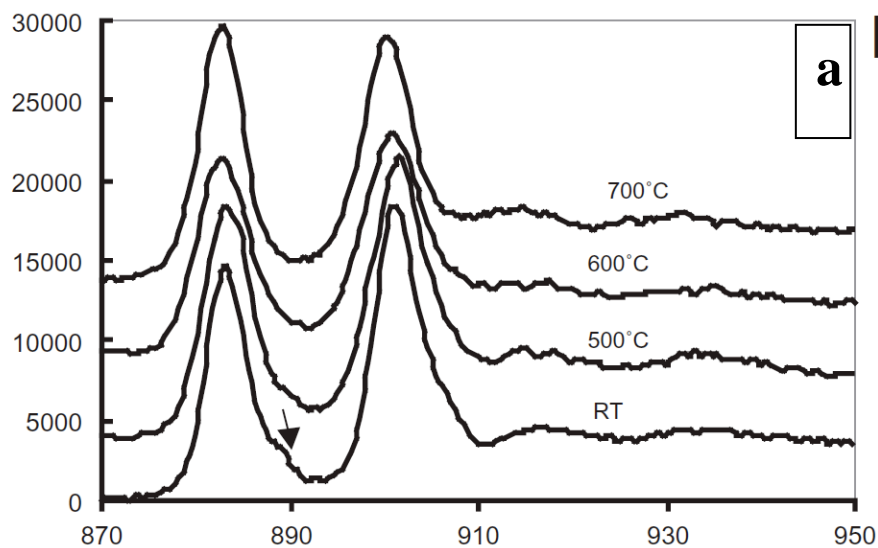


Figure 10. (a) Background-subtracted Ce  $M_{4,5}$  peaks, extracted from electron energy-loss spectroscopy data recorded during heating  $CeO_2$  nano particles. Note the change in relative white-line intensity with temperature and disappearance of the small shoulder, indicated by the arrow, with reduction. (b) Plot showing the relationship between Ce oxidation state and white line intensity ratio with temperature.

